High-End Manufacturing
https://www.sciltp.com/journals/hem

Article

Two-Dimensional Evolution of Thermomechanical Interfacial Stripping in Ultrafast Laser Processing of Metal/Polymer Layered Systems

Zhidong Huang [1,2,3], Yukui Cai [1,2,3,4,*], Teng Zhang [5], Yunlong Han [5], Yunqing Tang [1,2,3,4], Xing Li [1,2,3,4], Xiaoliang Liang [1,2,3,4] and Zhanqiang Liu [1,2,3,4]

[1] School of Mechanical Engineering, Shandong University, Jinan 250061, China
[2] Shandong Key Laboratory of High Performance Tools and System, Jinan 250061, China
[3] Key Laboratory of High Efficiency and Clean Mechanical Manufacture of Ministry of Education, Jinan 250061, China
[4] State Key Laboratory of Advanced Equipment and Technology for Metal Forming, Shandong University, Jinan 250061, China
[5] Aviation Key Laboratory of Science and Technology on High Performance Electromagnetic Windows, Research Institute for Special Structures of Aeronautical Composite, Aviation Industry Corporation of China, Ltd. (AVIC), Jinan 250023, China
* Correspondence: caiyukui@sdu.edu.cn

How To Cite: Huang, Z.; Cai, Y.; Zhang, T.; et al. Two-Dimensional Evolution of Thermomechanical Interfacial Stripping in Ultrafast Laser Processing of Metal/Polymer Layered Systems. *High-End Manufacturing* **2026**, *1*(1), 2.

Received: 16 August 2026
Revised: 8 October 2026
Accepted: 30 October 2026
Published: 6 November 2026

Abstract: Ultrafast laser etching of layered materials has found wide application in various fields, yet the laser-induced interaction mechanism at heterogeneous interfaces remains incompletely understood. While interfacial stripping has been recognized as a thermomechanical removal mechanism for metal/polymer layered systems, current numerical investigations are predominantly based on one-dimensional (1D) simulation frameworks, which neglect the spatial Gaussian profile of laser fluence and radial mass and energy transport. As a result, the spatial evolution of this mechanism under realistic laser irradiation remains unclear. Here, we extend the simulation from 1D to a fully coupled two-dimensional (2D) model incorporating spatial Gaussian energy deposition, and validate the mechanism via multipass laser ablation experiments. The results reveal that radial energy and mass transfer accelerate the relaxation of intense temperature and pressure gradients, converting fluence-partitioned localized removal into uniform stripping of the remaining film. Multipass scanning depth experiments confirm that the material removal efficiency at the interface is significantly higher than that in the initial pure metal ablation stage, verifying the transition of the removal mechanism. Furthermore, the critical thickness threshold for copper stripping under the applied laser parameters is measured to be 44 ± 1.1 μm, which is challenging to determine via simulation. These findings highlight the role of interfacial stripping in improving material removal efficiency during ultrafast laser processing of metal/polymer layered systems.

Keywords: femtosecond laser ablation; metal/GFRP laminated composites; molecular dynamics; TTM-MD

1. Introduction

Ultrafast laser etching of layered materials has emerged as a key manufacturing technique in different fields such as aerospace, microelectronics, and advanced communication systems [1–4]. In these high-precision applications, it remains challenging to selectively remove surface functional coatings without inducing degradation in heat-sensitive substrates. Among various manufacturing approaches, femtosecond (fs) laser ablation offers

Copyright: © 2026 by the authors. This is an open access article under the terms and conditions of the Creative Commons Attribution (CC BY) license (https://creativecommons.org/licenses/by/4.0/).
Publisher's Note: Scilight stays neutral with regard to jurisdictional claims in published maps and institutional affiliations.

exceptional spatial precision and minimal thermal diffusion, thus making it widely adopted for the precision etching of diverse layered material systems [5–7]. Nevertheless, it is difficult to achieve reliable process control because the transient thermomechanical response and removal mechanisms localized at these heterogeneous interfaces are still not fully understood [8–11].

Laser-induced material removal has traditionally been described as a thermal process in which absorbed energy drives melting and vaporization. The two-temperature model (TTM) is widely used to describe the nonequilibrium heat transfer between electrons and the lattice under ultrafast laser irradiation [1,2]. However, studies of layered materials [3,8] have shown that laser-induced stress can also play an important role in material removal. For example, He et al. [8] reported a transition from thermal ablation to stripping in multilayer coatings under nanosecond irradiation. These findings call for a coupled thermomechanical description of material removal that accounts for both heat transfer and stress-driven interfacial separation.

In recent years, the two-temperature model coupled with molecular dynamics (TTM-MD) has become a powerful tool for resolving microscopic ultrafast laser-matter interactions [12–14]. Unlike continuum approaches such as the finite element method, which usually require empirical failure criteria or temperature thresholds to impose material removal [15,16], the TTM-MD approach tracks nonequilibrium phase transitions, stress wave propagation, and material ejection at the atomic scale based purely on interatomic potentials. Using this approach, our previous study [17] identified interfacial stripping as a distinctive thermomechanical removal mechanism in metal/polymer layered systems. Unlike phase explosion or spallation, interfacial stripping is driven by the elastic rebound of the laser-compressed polymer substrate, which converts stored elastic energy into the kinetic energy of the remaining metallic film. The study also compared different pulse durations and showed that shorter pulses rapidly generate high pressures, enabling interfacial stripping at substantially lower fluences. This mechanical removal pathway enables efficient film removal with low energy input and limited substrate damage, demonstrating the advantages of ultrafast laser processing for layered materials.

Despite these advances, most TTM-MD simulations of femtosecond laser ablation have long been restricted to idealized one-dimensional (1D) models along the ablation depth direction to reduce computational cost [18–21]. Such simplification treats the laser as a homogeneous planar heat source, neglecting the spatial Gaussian distribution of laser fluence. Furthermore, due to the periodic boundary conditions applied along the lateral directions, radial energy and mass transport are ignored, including the relaxation of thermal and stress gradients, as well as the lateral material continuity [18,20,22]. As a result, the spatial evolution dynamics of interfacial stripping under realistic laser energy distributions have not been fully revealed. Wu and Zhigilei [23] constructed pseudo-two-dimensional (pseudo-2D) maps by combining a series of independent 1D simulation columns, which successfully predict spatial variations of material removal under different localized fluences. However, this approach still neglects lateral interactions such as radial stress relaxation and in-plane mechanical coupling. Fully coupled two-dimensional (2D) models are therefore needed, even though the micrometer-scale laser spots used in experiments must be downscaled to nanometer-scale molecular dynamics (MD) domains to remain computationally manageable [24,25].

Another critical challenge lies in bridging the dimensional gap between nanoscale MD simulations and macroscale experimental measurements, as it is difficult to characterize the dynamic behavior of interfacial stripping directly through physical experiments. Previous studies [17] addressed this issue via *in-situ* high-speed imaging of ablation ejection dynamics, providing qualitative and direct support for the onset of interfacial stripping. However, the maximum film thickness at which interfacial stripping can be triggered is still unknown, as it remains challenging for atomistic simulations to explore micrometer-scale boundaries due to computational constraints.

Here, we address these gaps through an integrated computational and experimental study focusing on the metal-clad GFRP framework. We first extend the TTM-MD framework from a 1D column to a 2D spatial domain incorporating a localized Gaussian beam profile. By comparing the full 2D simulation results with a pseudo-2D model composed of independent 1D columns, we systematically analyze how radial energy and stress transfer modulate the interfacial stripping process. Furthermore, we validate this mechanism qualitatively via a multipass laser ablation experiment on thick copper (Cu) films on GFRP substrates. By tracking the evolution of groove depth with increasing scan numbers, we capture the transition of removal mechanisms and identify the critical film thickness threshold for triggering interfacial stripping.

2. Methodology

2.1. Atomistic Modeling of the Metal/Epoxy Heterogeneous Interface

The GFRP substrate was fabricated by impregnating glass fiber fabrics with epoxy resin, followed by curing. For the nanoscale MD simulations, the focus was placed exclusively on the surface epoxy resin layer. The atomistic

model of the epoxy substrate was first constructed in Materials Studio 2020 and cross-linked via Perl scripts [26,27]. Specifically, bisphenol A diglycidyl ether (DGEBA) monomers and 1,3-benzenediamine (*m*-Phenylenediamine) curing agents were packed into a 4 nm × 4 nm × 2 nm amorphous cell at a 2:1 stoichiometric molar ratio with an initial density of 1 g/cm^3. After energy minimization and initial relaxation, the cross-linking reaction was performed at 580 K under the COMPASS II force field. The resulting cross-linked epoxy structure was then replicated to the target dimensions using periodic boundary conditions, and its potential function was converted to the consistent valence force field (CVFF). A subsequent 100-ps relaxation in the NPT ensemble (300 K, 1 atm) yielded an equilibrated polymer matrix.

Subsequently, a 50-nm-thick face-centered cubic (FCC) nickel (Ni) film was deposited atop the relaxed epoxy substrate. Ni was selected after comparing the electron thermal diffusivities of aluminium (Al), Cu, and Ni (Table S2, Supporting Information). Rapid heat diffusion in Al and Cu quickly smooths out the temperature gradients induced by Gaussian laser irradiation. Under the adopted parameters, the electron thermal diffusivity of Ni is approximately 1/60 of that of Al and 1/80 of that of Cu, allowing these gradients to persist within the nanoscale simulation domain. To eliminate unphysical atomic overlap at the heterogeneous interface, the assembled configuration was minimized using the conjugate gradient algorithm and subsequently equilibrated in the NPT ensemble for 100 ps.

A hybrid potential function was used because the system contains a metal, a polymer, and their heterogeneous interfaces. Interactions between Ni atoms were described using the embedded-atom method (EAM) potential [28]. The intra- and intermolecular interactions within the epoxy substrate were described by the CVFF [29]. The nonbonded interfacial interactions governing the adhesion strength were described by the 12-6 Lennard–Jones (L–J) potential, with cross-parameters determined using the Lorentz–Berthelot mixing rules. The details of these parameters were taken from Reference [30], which was specifically developed for metal and hybrid interfaces, as summarized in Table S1 (Supporting Information).

2.2. TTM-MD Coupling Model

Femtosecond-laser-induced ablation was simulated using the TTM-MD framework (Figure 1). The two-temperature model (TTM) describes nonequilibrium energy transfer between electrons and lattices under ultrafast irradiation [31], whereas MD resolves the subsequent atomistic thermal response and material removal. The entire simulation domain was overlaid with a discretized grid that coupled the two subsystems via electron–lattice energy exchange. This coupling was implemented in LAMMPS 22 July 2025 (Sandia National Laboratories, Albuquerque, NM, USA) by modifying the source code of the fix ttm/mod package [32,33].

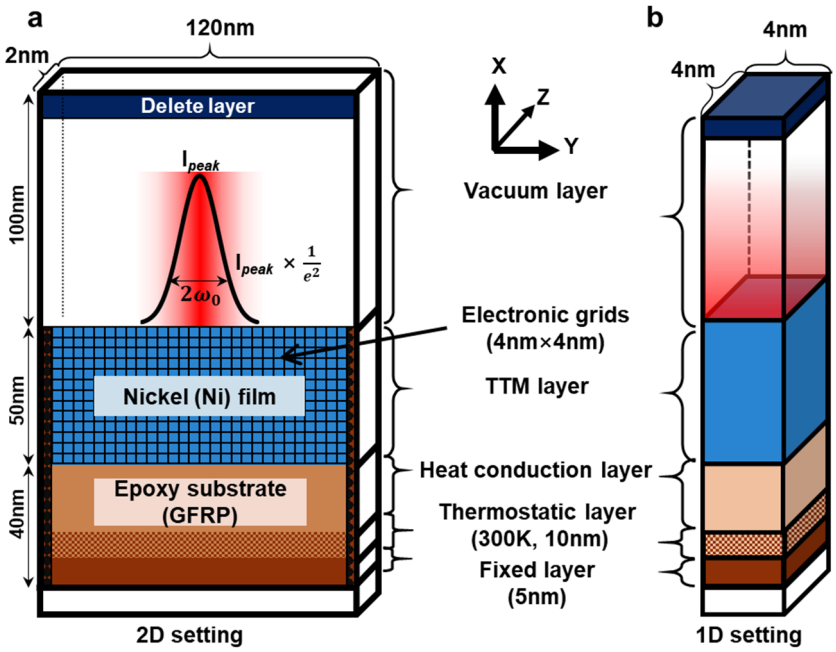


Figure 1. Schematic illustration of TTM-MD simulation. (**a**) 2D model with a spatial laser intensity distribution. (**b**) 1D localized model.

In the coupled TTM-MD framework, the electron temperature (T_e) was calculated based on a finite difference method (FDM) grid using the electron heat conduction equation:

$$C_e(T_e)\frac{\partial T_e}{\partial t} = \nabla[\kappa_e(T_e)\nabla T_e] - G(T_e - T_l) + S \quad (1)$$

where T, C, and κ represent temperature, heat capacity, and thermal conductivity, respectively. The subscripts "e" and "l" respectively refer to electrons and lattices. G and S represent the electron–phonon coupling coefficient and the laser heat source, respectively. Meanwhile, the lattice temperature (T_l) was directly determined by calculating the statistical thermal velocities of the MD atoms within each grid cell [18]. The heat transfer between the electron grid and the atomic ensemble was coupled via a local Langevin thermostat, which introduced a damping coefficient and a stochastic force into the atomic equations of motion. The corresponding electron–lattice coupling term was governed by the coupling factor described in [12,20]

$$\xi = \frac{G\sum_{k=1}^{n} V_N(T_e^k - T_i)}{n\sum_i m_i(v_i^T)^2} \quad (2)$$

where V_N is the volume of each cell used for FDM simulation, and N is the total number of FDM cells.

Regarding TTM parameters, the thermodynamic properties of the metallic films were adopted from refs. [34,35]. The temperature-dependent electron heat capacity (C_e) was determined by fitting first-principles calculation data [36], while the electron thermal conductivity (κ_e) was calculated as $\kappa_e = C_e \times D_e$, where D_e is the electron diffusion coefficient [37]. The electron–phonon coupling factor (G) was obtained from ref. [38]. The detailed thermodynamic parameters for the metals are summarized in Table S2 (Supporting Information).

In the 1D simulations, since the laser spot size is orders of magnitude larger than the optical penetration depth of the material, the radial variation in laser intensity within the nanoscale computational domain can be neglected. Consequently, the energy deposition simplifies to a 1D absorption profile along the beam incident direction (*x*-axis) governed by the Beer–Lambert law:

$$S(x) = \frac{I_0}{\delta_p}\exp\left(-\frac{x}{\delta_p}\right) \quad (3)$$

where I_0 is the absorbed power density at the material surface, x is the depth from the surface, and δ_p is the optical penetration depth.

To further elucidate the role of radial energy gradients, a 3D Gaussian heat source distribution was introduced by modifying the fixed ttm/mod source code. For a Gaussian beam, the volumetric heat source term at any spatial coordinate can be expressed as [24,25]

$$S(x,y,z) = \frac{I_{peak}}{\delta_p}\exp\left(-\frac{x}{\delta_p}\right)\cdot\exp\left(-\frac{2(y^2+z^2)}{w_0^2}\right) \quad (4)$$

where ω_0 denotes the beam waist radius at which the laser intensity drops to $1/e^2$ of its axial peak. In the code implementation, the input I_{peak} corresponds to the peak power density evaluated at the origin ($x = 0$, $y = 0$, and $z = 0$).

2.3. Model Configuration and Simulation Details

As shown in Figure 1, the simulation model is a layered structure along the laser incident direction (*x*-axis). A 100 nm vacuum layer was placed above the material surface to accommodate laser-induced surface expansion and atom ejection. An atom-deletion region was defined above this vacuum layer, and ejected atoms were deleted once they reached this boundary to prevent passage through the periodic boundary. The material bulk consists of a 50 nm metallic layer and a 40 nm epoxy substrate. A nonreflective boundary condition (NRBC) was applied to prevent laser-induced thermoelastic stress waves from reflecting off the bottom boundary and causing unphysical material spallation [37,39]. The bottom NRBC contained a Langevin thermostat layer held at 300 K to dissipate heat and stress, followed by a fixed atomic layer to maintain structural stability. A 5 nm fixed atomic zone was also applied at both lateral boundaries along the *y*-direction to represent confinement by the surrounding cold material. The electron subsystem was discretized into 50(*x*) × 30(*y*) × 1(*z*) finite-difference cells, each measuring 4 nm × 4 nm × 2 nm. Laser energy deposition began at the 25th grid layer along the *x*-axis, targeting the metal surface, and was coupled only to metallic atoms. The model is thin in the *z* direction (2 nm, with one electron-grid cell), and the spatial evolution investigated here is resolved in the *x*–*y* plane.

The laser pulse duration was set to 350 fs, consistent with experimental conditions. Since the electron–lattice coupling typically reaches equilibrium within tens of picoseconds (Figure 2d), the TTM module was enabled for the first 50 ps to capture the primary non-equilibrium heat transfer phase after laser absorption. Subsequently, the

TTM module was deactivated, and the system evolved in the microcanonical (NVE) ensemble for another 200 ps to track atomistic dynamics [19,37]. The time step was 0.2 fs. Temperature and stress fields were recorded using spatial binning. OVITO 3.13.0 was used to visualize atomic trajectories and lattice-defect evolution [40], and the centro symmetry parameter (CSP) was used to characterize phase transitions and structural defects [41,42].

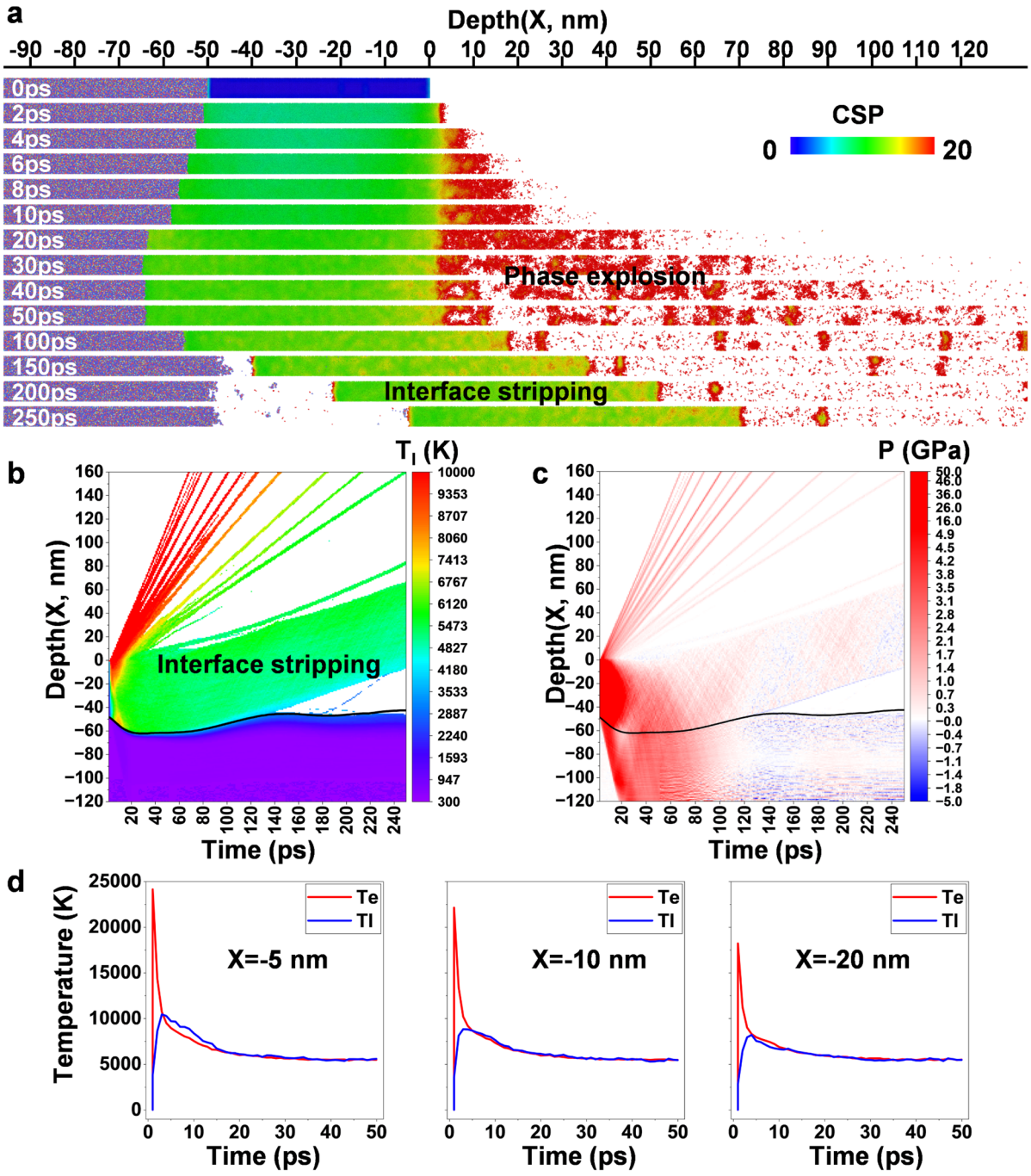


Figure 2. 1D TTM-MD simulation results of femtosecond laser irradiation at 0.15 J/cm^2. (**a**) Atomic snapshots. Spatiotemporal distributions of (**b**) lattice temperature and (**c**) pressure. The solid black lines in panels (**b**,**c**) denote the evolution of the metal/epoxy heterogeneous interface. (**d**) Transient profiles of electron temperature (T_e) and lattice temperature (T_l) at varied depths of x = −5, −10, and −20 nm, respectively.

2.4. Femtosecond Laser Processing Experiments

Micromachining experiments were performed using an infrared femtosecond laser system. The laser source delivered pulses at a central wavelength of 1030 nm, with a pulse duration of 350 fs and a maximum average power of 40 W. The beam was directed through a galvanometric scanner and focused onto the material surface

with a focal spot diameter of approximately 20 μm. Computer control of the galvanometric scanner enabled large-area patterning and selective etching of metallic films.

The samples were 105 μm-thick copper films clad on GFRP substrates, as illustrated in Figure S2 (Supporting Information). To fabricate grooves on the copper-clad GFRP, the femtosecond laser scanned a 0.3 mm-wide region using parallel hatch lines spaced by 15 μm. The processing parameters were fixed at an output power of 5.1 W, a scanning speed of 700 mm/s, and a pulse repetition frequency of 100 kHz. The number of scanning passes varied from 1 to 80.

After laser irradiation, optical microscopy was used to inspect groove morphology and surface damage. Confocal laser scanning microscopy (CLSM) was then used to measure cross-sectional profiles and groove depths. The centerline average roughness (R_a) along the scanning direction was also measured to evaluate removal uniformity. The detailed measurement methodology and standardization process are provided in Section S1 (Supporting Information).

3. Results and Discussion

3.1. Interfacial Stripping as a Thermomechanical Removal Mechanism

Interfacial stripping represents a thermomechanical-coupled removal mechanism driven by laser-induced stress in layered materials [17]. Figure 2a depicts TTM-MD snapshots of a 50 nm-thick Ni film irradiated at a laser fluence of 0.15 J/cm^2 with a 350-fs pulse width. Atoms are colored by CSP [41]: blue atoms (CSP 0–6) correspond to a highly ordered solid FCC lattice, green atoms (CSP 6–12) indicate the liquid phase (molten metal), and red atoms (CSP > 12) mark high-velocity vaporized or ejected clusters. Figure 2d shows the evolution of electron and lattice temperatures at different positions (x = −5, −10, and −20 nm). The electron–lattice relaxation process reaches an equilibrium before 15 ps at these locations. Therefore, limiting the TTM calculation time to 50 ps can accelerate the computation speed without compromising accuracy.

Initially, the metal maintains a perfect crystalline lattice (CSP = 0). By 2 ps, the 50 nm Ni film has melted through its full thickness. Concurrently, an intense compressive stress wave with a peak value of up to 50 GPa is generated near the irradiated surface, accompanied by a phase explosion that ejects small atomic clusters. Subsequently, this phase explosion expands and intensifies. Simultaneously, driven by both thermal expansion and the propagation of the laser-induced stress, the substrate is severely compressed and reaches its limit at approximately 30 ps. The compressed epoxy then begins to rebound and propel the metal layer forward. At t = 150 ps, interfacial stripping is initiated, and the remaining unablated metallic film is removed as an intact layer. As demonstrated in our previous study [17], the interfacial adhesion degrades drastically at the elevated temperature, thereby promoting this stripping behavior.

Compared to the removal of an 80 nm Al film, as reported in our previous study [17], the fundamental mechanism of Ni removal is found to be consistent. However, as Ni possesses lower thermal diffusivity and higher density (8.9 g/cm^3, roughly 3.3 times that of Al, which is 2.7 g/cm^3), the thermomechanical response of the Ni system is delayed under comparable energy input. As a result, interfacial stripping occurs at approximately 150 ps in the Ni film, compared with approximately 100 ps in the Al film.

3.2. Material Removal Mechanisms Under a Gaussian Energy Distribution

Previous Al/epoxy simulations show that the material removal mechanism transitions distinctly with varying local laser fluences [17]. Specifically, high fluences favor a thermal-dominated phase explosion, ejecting many highly thermalized nanoclusters (~1 nm), whereas low fluences tend to induce mechanical-dominated mechanisms such as spallation and interfacial stripping, producing larger clusters with lower ejection velocities. In the present study, an analogous physical picture is replicated in the ablation of Ni/epoxy, as shown in Figure 3 and Video S1.

Figure 3 presents the combined 1D simulation results under a spatial Gaussian energy distribution with a peak fluence I_{peak} of 0.73 J/cm^2 and a beam waist diameter of 22.6 nm. It should be noted that the nanoscale beam diameter is only a simplified configuration tailored for the MD domain, but cannot be directly scaled to micrometer-sized laser spots. As shown in Figure 3, three distinct ablation regimes are clearly identified along the radial direction based on the localized energy density. In the core region (within 6 nm from the beam center) with a local fluence of 0.42–0.73 J/cm^2, the material removal is entirely driven by a violent phase explosion. In the transition zone (ranging from 8 to 10 nm) with a local fluence of 0.15–0.27 J/cm^2, the material removal transitions to a mechanically dominated regime, featuring a mixture of spallation and interfacial stripping. Beyond a radial distance of 12 nm, where the local fluence drops below 0.08 J/cm^2, the metallic film fails to achieve complete detachment within the 200 ps simulation window despite the occurrence of minor localized spallation. Hence, the 1D results infer that the ablation behavior varies across different energy density zones.

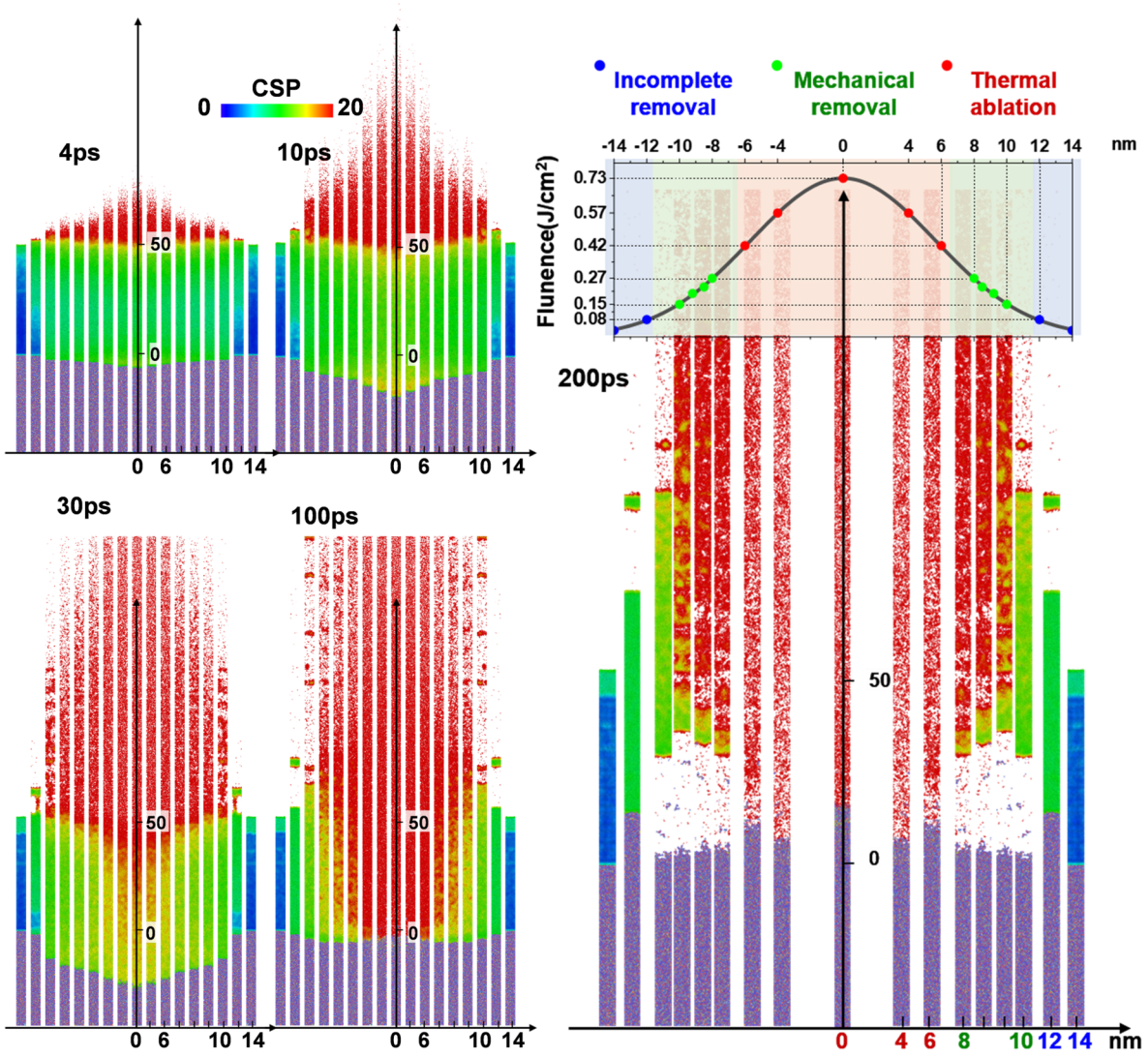


Figure 3. Pseudo-2D atomistic snapshots and corresponding removal mechanisms at different locations and corresponding fluences under a spatial Gaussian distribution. Note: For the high-fluence regions (0.42–0.73 J/cm^2), the epoxy substrate was fixed after ~150 ps to maintain computational convergence, without altering the established mechanisms. The corresponding dynamic process is available in Movie S1.

However, in 1D models with periodic boundary conditions, thermal conduction and material continuity along the radial direction are not considered. To elucidate how this radial mass and energy transport affect the removal process, we extended our investigation to 2D TTM-MD simulations using an identical peak fluence (0.73 J/cm^2) and beam waist diameter (22.6 nm). The corresponding CSP and pressure evolutions are displayed in Figures 4 and 5, respectively (see Video S2 in the Supporting Information).

The early-stage 2D response remains consistent with the local mechanisms inferred from the 1D simulations. At t = 1 ps, the film surface expands rapidly, and the ultrafast laser excitation induces a massive compressive shock wave with a peak pressure of 168 GPa. At t = 3 ps, phase explosion occurs within the central high-energy region, ejecting a massive amount of highly thermalized nanoclusters and rapidly relieving the surface pressure. At the same time, the stress wave within the bulk propagates both downward and laterally, reaching the metal/epoxy interface at t = 4 ps and initiating the compression of the underlying polymer substrate. At t = 25 ps, the surface metallic layer is removed via distinct mechanisms: phase explosion in the central high-energy zone and spallation in the peripheral low-energy zone. This confirms the fluence-dependent removal mechanisms exhibited by the 1D simulations in Figure 3.

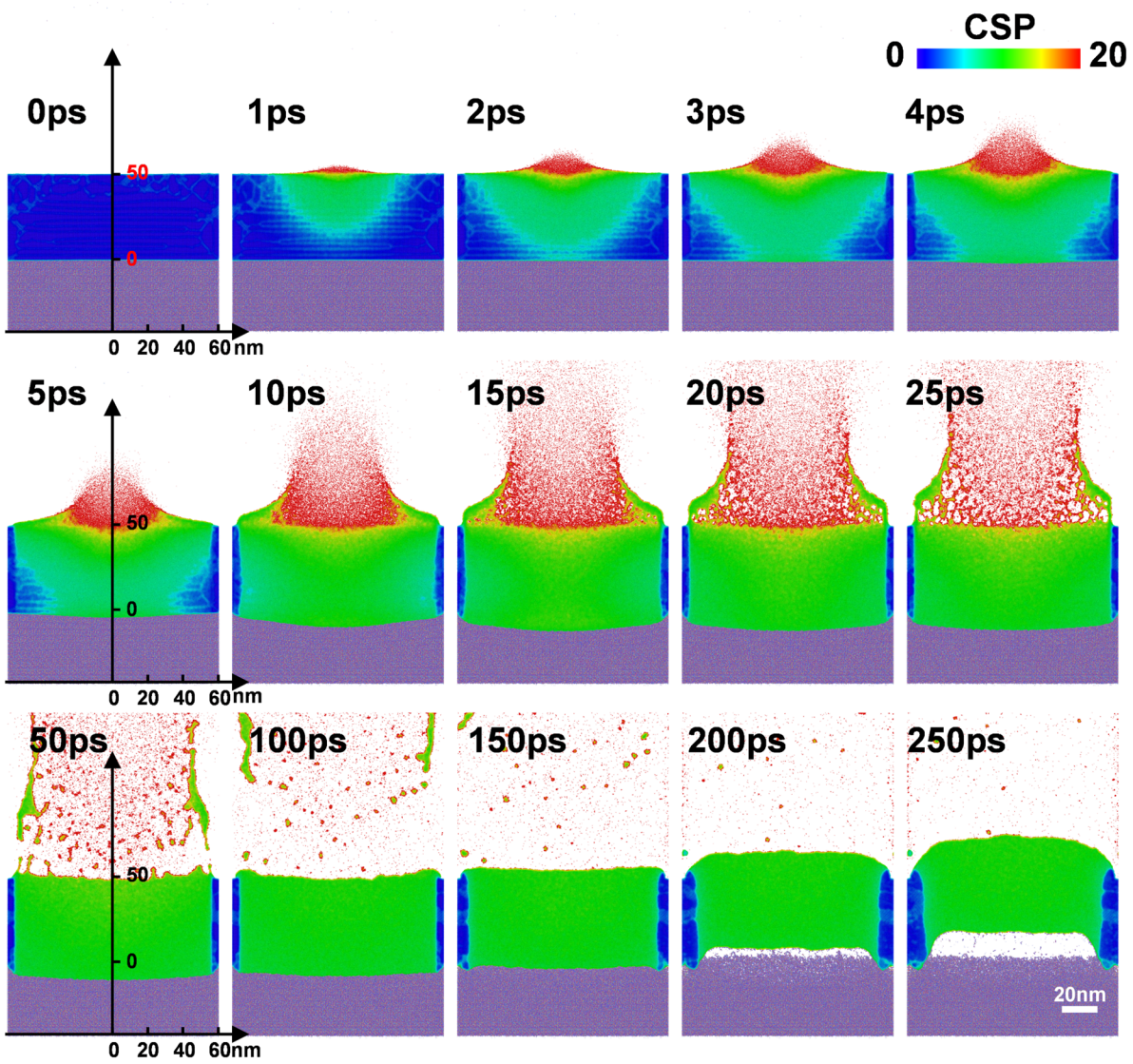


Figure 4. Atomistic snapshots of the CSP evolution during the 2D TTM-MD simulation under a spatial Gaussian energy distribution. The corresponding dynamic evolution is available in Movie S2.

The later-stage 2D response reveals the key effect of lateral continuity. Laser-induced stress compresses the substrate until the epoxy reaches its compression limit at $t \approx 50$ ps, and then begins to elastically rebound. At $t =$ 150 ps, the interface returns close to its original planar position; however, a severe tensile stress field develops within the interfacial region, marking the beginning of the interfacial stripping stage for the unablated film. Instead of directly flying off upon interface separation as seen in 1D models (Figure 2a), the remaining film in the 2D simulation is restricted by the fixed boundaries at both lateral edges. Consequently, at $t = 250$ ps, the film forms an arched profile, highly elevated in the center but pinned at the edges. Under this condition, complete material removal depends not only on the interfacial separation but also on overcoming its own material continuity to shear away from the surrounding cold zones. Therefore, the actual macroscopic stripping process is delayed compared to the idealized 1D predictions.

The comparative analysis reveals that although the fluence-dependent variations in removal mechanisms are still observed in the 2D simulation, they are confined to the topmost surface of the material. For the deeper metallic layers, the remaining film is stripped off from the interface entirely as a single unified body. Due to material continuity, the radial transfer of both mass and energy accelerates thermal relaxation, thereby smoothing the intense temperature and pressure gradients and leading to uniform material removal. Thus, the full 2D model complements the radial simplification deficiencies ignored in the 1D models. Specifically, the 1D results indicate that complete removal only occurs within a central radius of ~10 nm and exhibits a fluence-dependent partitioned removal mechanism, whereas the 2D simulation shows uniform stripping of the whole film across the entire 60 nm radius domain.

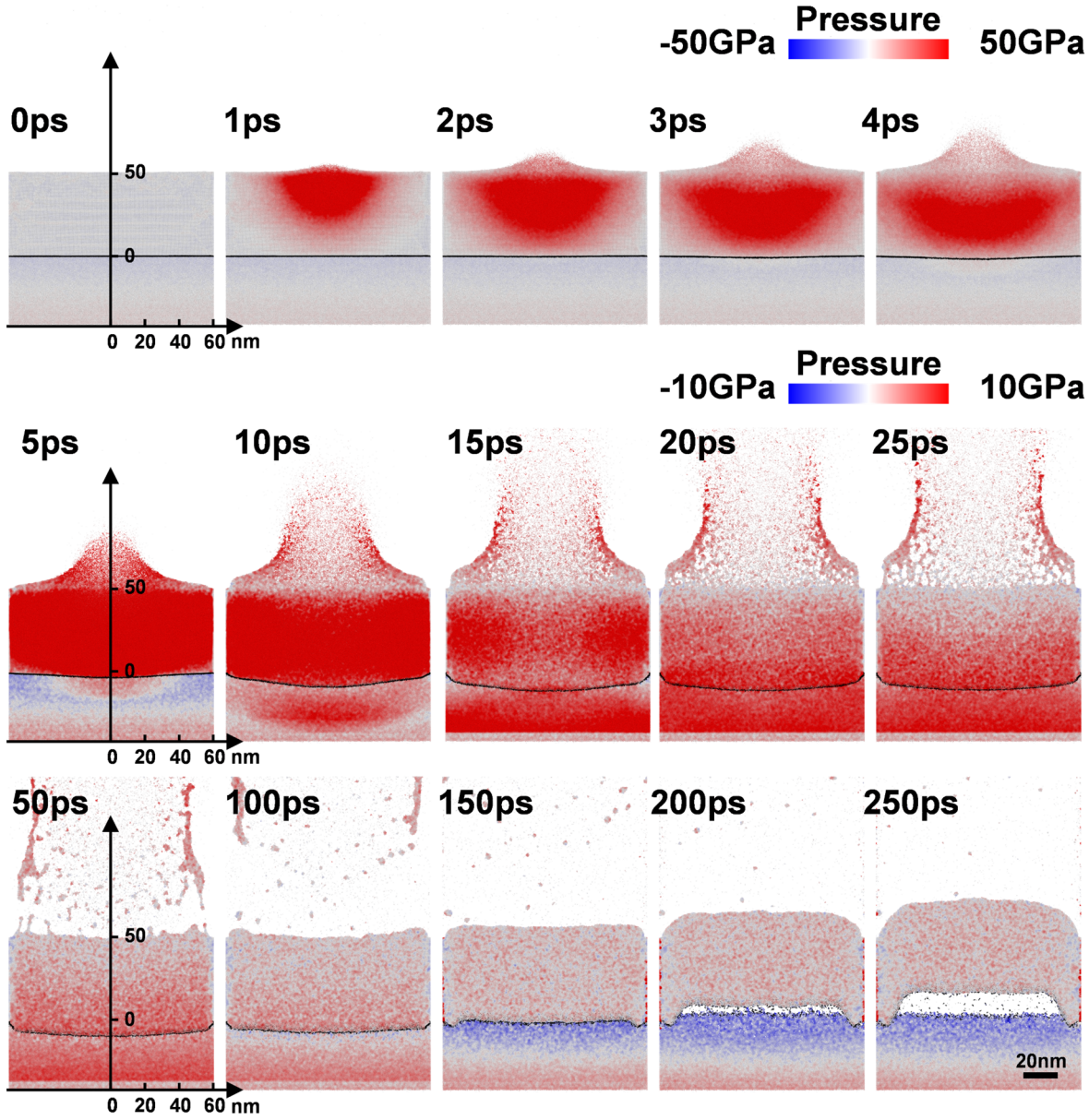


Figure 5. Atomistic snapshots of the pressure evolution during the 2D TTM-MD simulation under a spatial Gaussian energy distribution.

3.3. Experimental Validation via Multipass Laser Scanning

Our previous study [17] used *in situ* high-speed imaging to observe a clear change in ejection behaviour as laser removal approached the metal/polymer interface. Ablation of the pure metal mainly produced a fine plume, whereas removal near the interface produced larger, slower molten droplets. Together with atomistic cluster analysis, these observations provided direct, qualitative evidence for interfacial stripping. However, it remained unclear how thick the remaining metal film could be when stripping began. Although previous MD simulations demonstrated that interfacial stripping could be triggered at a remaining film thickness of approximately 1.5 μm [17], the computational cost prevented us from extending the simulations to thicker films to determine this limit.

To experimentally validate the interfacial stripping mechanism, systematic multipass laser scanning experiments were performed on a 105 μm-thick copper film clad on a GFRP substrate. Figure 6 displays the cross-sectional profiles and surface morphologies of the laser-ablated grooves under varying numbers of scanning passes with identical laser parameters. Figure 7 summarizes the cumulative removal depth and incremental depth per pass. Concurrently, the centerline average roughness (R_a) along the groove scanning direction was measured to characterize the uniformity of the material removal, presented as a shaded error band.

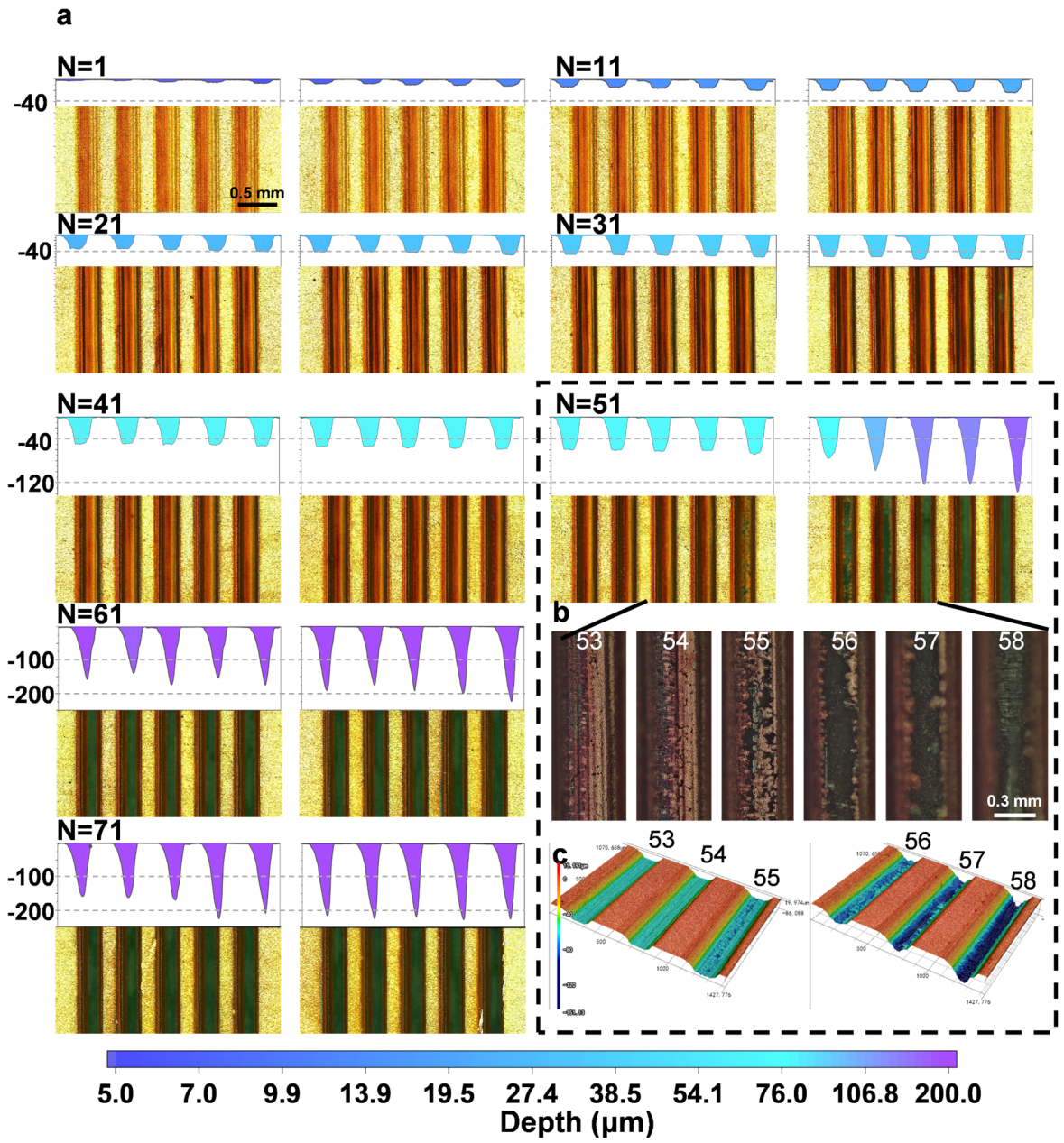


Figure 6. Morphological and profile evolution of the ablated grooves under multipass laser scanning. (**a**) Cross-sectional profiles and corresponding micrographs of the grooves as a function of scanning passes (*N*). (**b**) Magnified surface details and (**c**) 3D CLSM morphologies of the grooves ranging from $N = 53$ to $N = 58$, tracking the transition from metal ablation to substrate exposure.

As shown in Figure 7, the entire ablation process can be divided into three distinct stages. In the first stage, characterized by slow linear metal ablation (scans 1–54), the groove depth increases gradually and linearly. Each laser pass contributes an incremental depth of approximately 1.1 μm, reaching a cumulative depth of 60.8 μm after 54 scans. Figure 6a shows the corresponding optical micrographs with a progressive deepening of the ablation grooves. However, up to the 54th scan, the groove bottom remains entirely covered by the intact metallic copper film without any substrate exposure, maintaining its characteristic reddish metallic luster (Figure 6b).

In the second stage, characterized by rapid interfacial stripping (scans 54–57), the groove depth increases significantly. As shown in Figure 6b, localized stripping is initiated at the 55th scan, exposing localized regions of the underlying substrate. By the 57th scan, the remaining copper layer within the scanning zone is completely stripped away, fully exposing the substrate beneath. Concurrently, the total removal depth reaches 97.5 μm, which closely approaches the initial film thickness of 105 μm. This stage removes approximately 36.7 μm within only three scans, whereas the first 54 scans remove a cumulative depth of 60.8 μm. This shows a huge disparity in removal efficiency, confirming that the ablation mechanism at the interface is distinct from that of the bulk metal.

In addition, this approach successfully determines the critical thickness threshold, which has been challenging to estimate previously due to simulation scale constraints. Figure 6 shows that local substrate exposure first appears after pass 55, placing the onset of interfacial stripping between passes 54 and 55. Subtracting the removal depth after pass 54 (60.8 μm) from the nominal initial copper thickness (105 μm) gives an estimated remaining thickness of 44.2 μm. Using the average removal depth per pass before stripping (approximately 1.1 μm) to represent the thickness resolution, we estimate the onset thickness as 44 ± 1.1 μm under the present processing conditions (5.1 W, 100 kHz, 700 mm/s, 350 fs, and 1030 nm). Additional uncertainty may arise from substrate unevenness (Figure S2) and accumulated thermal damage to the substrate; these contributions are not included in the ±1.1 μm term.

In the third stage, characterized by over-ablation of the substrate (scans 57–80), the groove depth increases at an even higher rate but randomly, with severe fluctuations. As shown in Figure 6b, by the 58th scan, the laser interacts directly with the surface epoxy resin, triggering its rapid thermal decomposition and exposing the underlying reinforcing woven glass fibers. This phenomenon indicates a narrow processing window for achieving complete film removal with minimal substrate damage; a single additional laser scan can induce severe degradation of the resin matrix. Because of the orthogonal interlacing of the woven glass fibers, the exposed substrate possesses an inherently nonuniform, periodic mesh-like profile (Figure S1d). The inherent nonuniformity further exacerbates localized ablation discrepancies. As displayed in Figure 7b, the error bars (R_a) of the removal depth expand drastically at this stage.

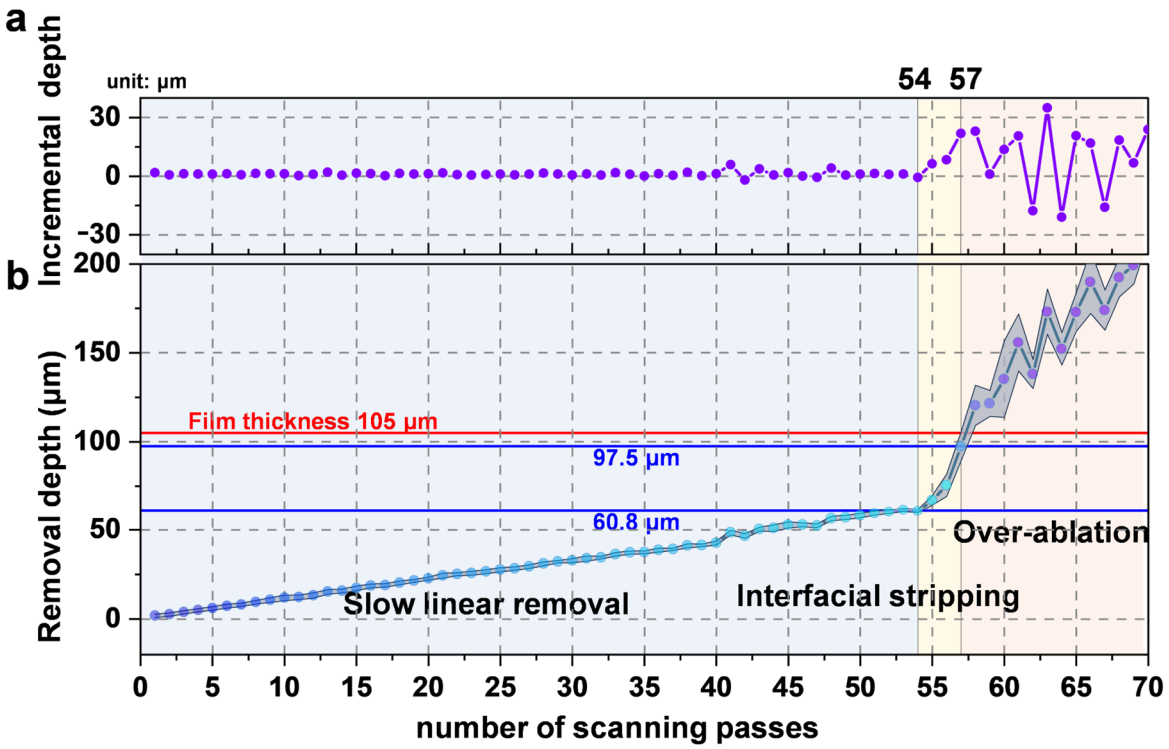


Figure 7. Evolution of removal depth with increasing scanning passes. (**a**) Incremental depth per pass; (**b**) cumulative removal depth, categorized into three regimes: slow linear removal, interfacial stripping (bounded between 60.8 and 97.5 μm), and over-ablation. The red horizontal line indicates the initial copper film thickness (105 μm).

4. Conclusions

This study extends the analysis of thermomechanical interfacial stripping to two-dimensional spatial evolution under a Gaussian energy distribution. Comparison between a pseudo-2D assembly of independent 1D simulations and a laterally coupled 2D model shows that radial energy and mass transfer accelerate the relaxation of the intense energy gradient distribution. This drives the material to be removed collectively through entirely interfacial stripping, rather than the fluence-partitioned removal predicted by 1D simulations. Multipass laser scanning depth experiments reveal that the material removal efficiency at the interface is significantly higher than that at the initial pure metal ablation stage, confirming a distinct transition in the removal mechanism. Under specified experimental parameters, the critical threshold thickness for the stripping of the copper film from the GFRP substrate is measured experimentally to be ~44 ± 1.1 μm. This result shows that stripping can begin while

tens of micrometers of metal remain, extending the understanding of its onset beyond the scale accessible to the present atomistic model. Together with our previous findings [17], these results highlight the potential of interfacial stripping to improve removal efficiency and alleviate the trade-off between complete film removal and substrate protection.

Supplementary Materials

The additional data and information can be downloaded at: https://media.sciltp.com/articles/others/261105 1605519707/HEM-26080121-SI.zip. Figure S1: Standardized measurement protocol for groove depth and uniformity. (**a**) Surface topography and raw depth data of the groove. (**b**) Standardization of the cross-sectional profile averaging method. (**c**,**d**) Assessment criteria for depth uniformity based on the bottom roughness (R_a) along the groove scanning direction. Figure S2: Cross-sectional micrograph for measuring the thickness of the Cu film layer (with a thickness range of approximately 105–112 μm). Table S1: Lennard–Jones (12-6) potential parameters for Al, Ni, and Cu (metal units) [1]. Table S2: Thermodynamic parameters of metal. Video S1: Atomistic snapshots of combined 1D simulation. Video S2: Atomistic snapshots of fully coupled 2D model. References [43,44] are cited in the Supplementary Information.

Author Contributions

Z.H.: Methodology, software, investigation, formal analysis, writing—original draft preparation, writing—review and editing; Y.C.: Conceptualization, supervision, project administration, writing—review and editing; T.Z.: Conceptualization, validation, writing—review and editing; Y.H.: Conceptualization, validation, writing—review and editing; Y.T.: Methodology, visualization, writing—review and editing; X.L. (Xing Li): Methodology, formal analysis, writing—review and editing; X.L. (Xiaoliang Liang): Methodology, validation, writing—review and editing; Z.L.: Resources, supervision, project administration. All authors have read and agreed to the published version of the manuscript.

Funding

The research is funded by the Jinan Science and Technology Bureau (202333034), Key R&D Program of Shandong Province, China (2025CXGC010216), and the Shandong Province Key Research and Development Plan (2024JMRH0308). The authors also acknowledge the support of the Scientific Research Innovation Team of Young Scholars in Colleges and Universities of Shandong Province (2020KJB001), and the Shandong Key Laboratory of High Performance Tools and System.

Institutional Review Board Statement

Not applicable.

Informed Consent Statement

Not applicable.

Data Availability Statement

The data that support the findings of this study are available from the corresponding author upon reasonable request.

Conflicts of Interest

The authors declare no conflicts of interest. Given the role as an Editorial Board Member, Yukui Cai had no involvement in the peer review of this paper and had no access to information regarding its peer-review process. Full responsibility for the editorial process of this paper was delegated to another editor of the journal.

Use of AI and AI-Assisted Technologies

During the preparation of this work, the authors used ChatGPT (OpenAI) to assist with language editing and manuscript preparation. After using this tool, the authors reviewed and edited the content as needed and take full responsibility for the content of the published article.

References

1. Gao, L.; Zhang, Q.; Gu, M. Femtosecond laser micro/nano processing: From fundamental to applications. *Int. J. Extrem. Manuf.* **2025**, *7*, 022010. https://doi.org/10.1088/2631-7990/ad943e.
2. Huang, J.; Xu, K.; Xu, S. Super-resolution laser machining. *Int. J. Mach. Tools Manuf.* **2025**, *205*, 104246. https://doi.org/10.1016/j.ijmachtools.2025.104246.
3. Zhao, Y.; Li, J.; Luo, M.; et al. Ultrafast Laser Fabrication of a Flexible Sensor by Selective Ablation for a Dynamic Tactile Recognition System. *ACS Appl. Mater. Interfaces* **2025**, *17*, 47130–47140. https://doi.org/10.1021/acsami.5c07670.
4. Wang, S.; Li, T.; Liu, T.; et al. Low-cost Fabrication of Isooctyl Acrylate Polymer Periodic Structures by Laser Interference Photocuring. *Nanomanuf. Metrol.* **2025**, *8*, 3. https://doi.org/10.1007/s41871-025-00251-2.
5. Zhu, P.; Boyce, A.; Daemi, S.R.; et al. A groovy laser processing route to achieving high power and energy lithium-ion batteries. *Energy Storage Mater.* **2024**, *69*, 103373. https://doi.org/10.1016/j.ensm.2024.103373.
6. Zhou, G.X.; Zhao, Z.; Zhang, Y.Z.; et al. Printing and electromagnetic characteristics of 3D printing frequency selective surface using graphene. *J. Mater. Sci. Technol.* **2022**, *111*, 49–56. https://doi.org/10.1016/j.jmst.2021.09.041.
7. Yang, G.; Liu, Y.; Liu, L.; et al. Mechanism and technology of laser adaptive cleaning for aircraft skin multilayer coatings of Airbus A320. *J. Manuf. Process.* **2025**, *135*, 230–239. https://doi.org/10.1016/j.jmapro.2025.01.050.
8. He, Z.; Zheng, S.; Shen, Y.; et al. Laser-induced layer-by-layer removal and thermo-mechanical action mechanisms of FeCo-based multilayer wave-absorbing coatings. *J. Mater. Sci. Technol.* **2024**, *190*, 10–23. https://doi.org/10.1016/j.jmst.2023.12.030.
9. Huang, Z.; Cai, Y.; Xue, F.; et al. Precise patterning of carbon films on polyethylene terephthalate polymer substrates using femtosecond lasers. *Appl. Surf. Sci.* **2023**, *638*, 158113. https://doi.org/10.1016/j.apsusc.2023.158113.
10. Yang, G.; Ding, Y.; Liu, L.; et al. Mechanism and technology of laser selective removal of multilayer materials. *J. Mater. Process. Technol.* **2023**, *312*, 117868. https://doi.org/10.1016/j.jmatprotec.2023.117868.
11. Zheng, C.; Cai, Y.; Zhang, P.; et al. Femtosecond laser precision machining of carbon film based on aramid paper substrate. *J. Manuf. Process.* **2024**, *119*, 57–65. https://doi.org/10.1016/j.jmapro.2024.03.061.
12. Ivanov, D.S.; Zhigilei, L.V. Combined atomistic-continuum modeling of short-pulse laser melting and disintegration of metal films. *Phys. Rev. B* **2003**, *68*, 064114. https://doi.org/10.1103/physrevb.68.064114.
13. Zhou, Y.; Wang, X.; Lu, Z.; et al. Thermal stress wave-driven regime in femtosecond laser-induced nanomaterial transfer revealed by ultrafast electron microscopy and atomic simulation. *Int. J. Mach. Tools Manuf.* **2026**, *216*, 104366. https://doi.org/10.1016/j.ijmachtools.2026.104366.
14. Liu, H.; Xie, W.; Ding, Y.; et al. Review of molecular dynamics simulations in laser-based micro/nano-fabrication. *Nanoscale* **2024**, *16*, 21189–21215. https://doi.org/10.1039/d4nr03305a.
15. Wang, C.; Cai, Y.; Li, J.; et al. Numerical simulation and experimental study of femtosecond laser ablation of copper: A two-temperature model with temperature-dependent properties and multiple phase transitions. *Opt. Laser Technol.* **2024**, *171*, 110335. https://doi.org/10.1016/j.optlastec.2023.110335.
16. Ran, J.; Zhang, F.; Chen, C.; et al. A Multiphysics-Coupled 3D Visualization Model for Controlling Ultrafast Laser-Induced Micro-Hole Morphology on Monocrystalline Silicon. *Nanomanuf. Metrol.* **2026**, *9*, 12. https://doi.org/10.1007/s41871-026-00293-0.
17. Huang, Z.; Feng, Z.; Cai, Y.; et al. Atomistic insights of thermomechanical interfacial stripping—A pathway to low-damage femtosecond laser processing of layered materials. *J. Mater. Sci. Technol.* **2026**, *266*, 92–103. https://doi.org/10.1016/j.jmst.2025.12.035.
18. Xie, J.; Yan, J.; Zhu, D.; et al. Atomic-Level Insight into the Formation of Subsurface Dislocation Layer and Its Effect on Mechanical Properties During Ultrafast Laser Micro/Nano Fabrication. *Adv. Funct. Mater.* **2022**, *32*, 2108802. https://doi.org/10.1002/adfm.202108802.
19. Lin, G.; Jiang, L.; Hu, J.; et al. Transient electron properties and phase change in femtosecond laser processing of NiTi alloy: Multiscale simulation and experimental investigation. *J. Mater. Sci. Technol.* **2026**, *252*, 190–205. https://doi.org/10.1016/j.jmst.2025.06.025.
20. Zhou, Y.; Wu, D.; Luo, G.; et al. Efficient modeling of metal ablation irradiated by femtosecond laser via simplified two-temperature model coupling molecular dynamics. *J. Manuf. Process.* **2022**, *77*, 783–793. https://doi.org/10.1016/j.jmapro.2022.03.048.
21. Zhou, S.; Shen, H. Study on deformations of gold film induced by ultrafast laser at GHz burst mode. *J. Manuf. Process.* **2022**, *84*, 469–480. https://doi.org/10.1016/j.jmapro.2022.10.028.
22. Lin, G.; Jiang, L.; Ji, P.; et al. Ultrafast melting, spallation, and phase explosion in femtosecond laser processing on nickel film surface investigated by atomistic simulation and transient reflectivity microscopy. *Opt. Laser Technol.* **2025**, *180*, 111404. https://doi.org/10.1016/j.optlastec.2024.111404.
23. Wu, C.; Zhigilei, L.V. Microscopic mechanisms of laser spallation and ablation of metal targets from large-scale molecular dynamics simulations. *Appl. Phys. A* **2014**, *114*, 11–32. https://doi.org/10.1007/s00339-013-8086-4.

24. Yao, J.; Qi, D.; Liang, H.; et al. Exploring Femtosecond Laser Ablation by Snapshot Ultrafast Imaging and Molecular Dynamics Simulation. *Ultrafast Sci.* **2022**, *2022*, 9754131. https://doi.org/10.34133/2022/9754131.
25. Yang, D.; Zhang, M.; He, Z.; et al. Ultrafast heat transfer and microstructural evolution of Inconel 718 alloy under femtosecond laser processing. *Int. J. Heat Mass Transf.* **2026**, *256*, 128016. https://doi.org/10.1016/j.ijheatmasstransfer.2025.128016.
26. Xie, J.; Liu, Z.; Tian, H.; et al. Influence of water penetration on glass fiber-epoxy resin interface under electric field: A DFT and molecular dynamics study. *J. Mol. Liq.* **2023**, *385*, 122346. https://doi.org/10.1016/j.molliq.2023.122346.
27. Shokuhfar, A.; Arab, B. The effect of cross linking density on the mechanical properties and structure of the epoxy polymers: Molecular dynamics simulation. *J. Mol. Model.* **2013**, *19*, 3719–3731. https://doi.org/10.1007/s00894-013-1906-9.
28. Foiles, S.M.; Baskes, M.I.; Daw, M.S. Embedded-atom-method functions for the fcc metals Cu, Ag, Au, Ni, Pd, Pt, and their alloys. *Phys. Rev. B* **1986**, *33*, 7983–7991. https://doi.org/10.1103/physrevb.33.7983.
29. Dauber-Osguthorpe, P.; Roberts, V.A.; Osguthorpe, D.J.; et al. Structure and energetics of ligand binding to proteins: *Escherichia coli* dihydrofolate reductase-trimethoprim, a drug-receptor system. *Proteins Struct. Funct. Bioinform.* **1988**, *4*, 31–47. https://doi.org/10.1002/prot.340040106.
30. Heinz, H.; Vaia, R.A.; Farmer, B.L.; et al. Accurate Simulation of Surfaces and Interfaces of Face-Centered Cubic Metals Using 12–6 and 9–6 Lennard-Jones Potentials. *J. Phys. Chem. C* **2008**, *112*, 17281–17290. https://doi.org/10.1021/jp801931d.
31. Anisimov, S.I.; Kapeliovich, B.L.; Perelman, T.L. Electron emission from metal surfaces exposed to ultrashort laser pulses. *Zh. Eksp. Teor. Fiz.* **1974**, *66*, 375–377.
32. Duffy, D.M.; Rutherford, A.M. Including the effects of electronic stopping and electron–ion interactions in radiation damage simulations. *J. Phys. Condens. Matter* **2007**, *19*, 016207. https://doi.org/10.1088/0953-8984/19/1/016207.
33. Thompson, A.P.; Aktulga, H.M.; Berger, R.; et al. LAMMPS—A flexible simulation tool for particle-based materials modeling at the atomic, meso, and continuum scales. *Comput. Phys. Commun.* **2022**, *271*, 108171. https://doi.org/10.1016/j.cpc.2021.108171.
34. Li, C.; Liang, H.; Yang, Y.; et al. Ultrafast Modulation of the Molten Metal Surface Tension under Femtosecond Laser Irradiation. *Chin. Phys. Lett.* **2022**, *39*, 077901. https://doi.org/10.1088/0256-307x/39/7/077901.
35. Lin, Z.; Zhigilei, L.V. Temperature dependences of the electron–phonon coupling, electron heat capacity and thermal conductivity in Ni under femtosecond laser irradiation. *Appl. Surf. Sci.* **2007**, *253*, 6295–6300. https://doi.org/10.1016/j.apsusc.2007.01.032.
36. Lin, Z.; Zhigilei, L.V.; Celli, V. Electron-phonon coupling and electron heat capacity of metals under conditions of strong electron-phonon nonequilibrium. *Phys. Rev. B* **2008**, *77*, 075133. https://doi.org/10.1103/physrevb.77.075133.
37. Iabbaden, D.; Amodeo, J.; Fusco, C.; et al. Molecular dynamics simulation of structural evolution in crystalline and amorphous CuZr alloys upon ultrafast laser irradiation. *Phys. Rev. Mater.* **2022**, *6*, 126001. https://doi.org/10.1103/physrevmaterials.6.126001.
38. Kabanov, V.V. Electron-electron and electron-phonon relaxation in metals excited by optical pulse. *Low Temp. Phys.* **2020**, *46*, 414–419. https://doi.org/10.1063/10.0000874.
39. Schäfer, C.; Urbassek, H.M.; Zhigilei, L.V.; et al. Pressure-transmitting boundary conditions for molecular-dynamics simulations. *Comput. Mater. Sci.* **2002**, *24*, 421–429. https://doi.org/10.1016/s0927-0256(01)00263-4.
40. Stukowski, A. Visualization and analysis of atomistic simulation data with OVITO–the Open Visualization Tool. *Model. Simul. Mater. Sci. Eng.* **2010**, *18*, 015012. https://doi.org/10.1088/0965-0393/18/1/015012.
41. Ye, F.; Chen, Y.; Cai, L.; et al. Molecular Dynamics Simulation Study on Ablation Threshold of Aluminum Film under Femtosecond Laser Irradiation (In Chinese). *Chin. J. Lasers* **2024**, *51*, 1602408. https://doi.org/10.3788/cjl231243.
42. Kelchner, C.L.; Plimpton, S.J.; Hamilton, J.C. Dislocation nucleation and defect structure during surface indentation. *Phys. Rev. B* **1998**, *58*, 11085–11088. https://doi.org/10.1103/physrevb.58.11085.
43. Vestentoft, K.; Balling, P. Formation of an extended nanostructured metal surface by ultra-short laser pulses: Single-pulse ablation in the high-fluence limit. *Appl. Phys. A* **2006**, *84*, 207–213. https://doi.org/10.1007/s00339-006-3602-4.
44. Xiong, Q.; Li, Z.; Kitamura, T. Effect of Crystal Orientation on Femtosecond Laser-Induced Thermomechanical Responses and Spallation Behaviors of Copper Films. *Sci. Rep.* **2017**, *7*, 9218. https://doi.org/10.1038/s41598-017-09559-6.